Soft Matter

ROYAL SOCIETY OF CHEMISTRY

PAPER

Published on 29 July 2026

Cite this: *Soft Matter*, 2026, **22**, 5245

Experimental automation for high-throughput collection of phase behavior and dynamic light scattering data for thermally-responsive polymers

Paul F. Salipante, †*[a] Phillip D. Pickett, †[ab] Austin Gallegos,[b] Colin McCarragher,[a] Steven D. Hudson [a] and Vivek M. Prabhu *[a]

Many responsive polymeric systems, important for pharmaceutical formulations, exhibit complex phase behavior which require both large and precise experimental data sets for identifying phase boundaries between various self-assemblies, morphologies, and solution properties. Datasets of these polymeric systems are often limited by the quantity of materials and the time required to prepare samples and collect data. Here we develop automated methods for sample preparation and analysis while using initial sample volumes on the order of 100 μL. This volume was small enough to enable a dataset of a model monoclonal antibody protein solution. Two sample-delivery approaches (syringe- or pneumatic-based) are used to control the flow and mixing within the same measurement platform. The sample is appropriately delivered to a commercial low-volume temperature-controlled spectroscopic flow cell for characterization using in-line ultraviolet-visible spectroscopy, turbidity, dynamic light scattering, and a separate microcapillary rheometer for viscosity measurements. This approach can be further optimized to expedite structure–property datasets for the development of materials with targeted properties.

Received 4th May 2026,
Accepted 20th July 2026

DOI: 10.1039/d6sm00413j

rsc.li/soft-matter-journal

1 Introduction

There is widespread interest in generating systematic studies of structure, phase behavior, and dynamics of stimuli-responsive (co)polymers to achieve better modeling of material properties under various solution conditions. The use of automation for novel formulation discovery is particularly relevant for characterizing multi-component systems with complex phase diagrams.[1] Automation of laboratory tasks enables improvements to collection time, higher resolution, and potentially less cost than is feasible with manual operation. These methods also offer potential improvements in measurement repeatability as automated procedures are designed to reduce human error. This is particularly important whenever polymer systems have many features that make measurements difficult, such as phase boundaries that are sensitive to small changes in concentration or solution conditions.[2–5] Automation techniques can also be adapted to include machine learning techniques to improve the speed and efficiency of measurements for characterization of phase behavior.[6]

Many automated sample handling, mixing, and characterization methods have been combined for various chemical applications, including multicomponent mixtures and chemical synthesis.[7–10] A critical aspect for sample preparation is a reliable mixing procedure, which is typically performed within pipettes, syringes, or in static mixers.[11–14] The mixed samples are often then characterized in various chambers, such as a well-plate system,[15] or delivered to a beamline flow cell, such as neutron scattering or X-ray scattering.[16] Peristaltic or isocratic pumps have also been combined with light scattering that drive a sample through a flow cell to obtain a time-dependent size-measurement during a reaction or dilution.[17,18] Other continuous flow devices at the millifluidic scale have incorporated active in-line mixing and characterization with dynamic light scattering (DLS) for particle synthesis and characterization.[19,20] This approach is limited by the accuracy of DLS measurements under continuous flow conditions. This effect can be mitigated by either limiting the flow rate to be below a critical value, which was characterized by Destremaut *et al.*,[21] or by modeling the flow effect on the correlation function to extract an accurate size measurement.[22] Despite the advancements in materials discovery and characterization these methods have enabled, the volume required for these techniques is typically at least on the order of milliliters and can reach liter scale. Some of these methods can be adapted for sub-milliliter volumes, such as using electrospraying in multiwell plates,[23] but are best suited for low viscosity solutions, *viz.* mPa s

[a] *NIST Polymers & Complex Fluids Group, 100 Bureau Dr, Gaithersburg, MD 20899, USA. E-mail: vivek.prabhu@nist.gov, paul.salipante@nist.gov; Fax: +1(301)975-4924; Tel: +1(301)975-2820*

[b] *Dosage Form Design and Development, Biopharmaceuticals Development, AstraZeneca, Gaithersburg, Maryland, USA*

† These authors contributed equally to this work.

range.[24] For certain materials, such as high-value low-volume products such as protein solutions or research-stage synthesized molecules, the large sample volumes required to conduct assays may be prohibitive.

Rheological and scattering characterization of small volumes requires specialized techniques for both fluid handling and measurement methods, typically requiring minimum sample volumes of approximately 100 μL.[25,26] Microfluidic techniques are often used to achieve these volume requirements,[27,28] and sample mixing approaches using valve control to mix multiple fluid components.[29] Sample volumes can be reduced further through compartmentalization of samples in drops. For instance, multicomponent drops generated in a microfluidic junction were stored in a glass capillary and used to measure the phase diagrams of thermoresponsive polymers using small angle light scattering (SALS).[30–32] Microfluidic drop traps also have been used to measure the rheology of protein solutions using multiple-particle-tracking microrheology and a temperature gradient was applied to characterize the phase behavior.[33,34] The carrier fluid approach provides many flexibilities, but also a need to understand the interfaces between carrier fluid and drops, undesirable solubility and diffusional mixing and composition broadening. Drop-based approaches work well for certain characterization techniques, while continuous phase delivery provides a simpler setup and more flexibility with existing characterization techniques.

Here we aim to reduce the volume required for solution characterization by DLS, turbidity, ultraviolet-visible (UV-vis) spectroscopy, and small-volume microcapillary rheometry. We demonstrate two techniques for fluid delivery of thermoresponsive polymers and protein solutions while using less than 1 mL of an initial stock sample. The first approach uses multiple syringes in combination with a microfluidic mixer and a fluidic valve to deliver a mixed sample and displacing the previous sample in the flow line. The second approach uses pneumatic controls to deliver fluid in a sample reservoir to a flow cell and then return the sample to the reservoir for dilution. The accuracy of the nominal concentration of the resulting samples from these two methods is evaluated using UV-vis spectroscopy. The sample phase behavior and properties are characterized in a customized DLS setup with a fixed scattering angle of 90° and simultaneous transmission intensity measurement. The cloud-point temperature phase behavior and size characteristics of thermoresponsive polymers are measured, including poly(*N*-isopropylacrylamide) (pNIPAM), a well-defined polyzwitterion poly(3-(acrylamidopropyl-dimethylammonium) propyl-1-sulfonate) (pAPAPS), and block copolymers of these two polymers, pNIPAM-*b*-pAPAPS. The measurement approach is highlighted, and the results are validated and harmonized by the available literature for pNIPAM.[3,35] Finally, we test the main goals for automation of small-volumes with minimal manual intervention to quantify high-value monoclonal antibody protein concerning the diffusion interaction parameter, k_D, that is derived from DLS measurements and the concentration dependent viscosity using a small volume microcapillary rheometer.[28]

2 Methods

2.1 Automated fluid control

The different combinations of experimental setups are shown in Fig. 1. The syringe-driven flow is used for delivery to a cuvette flow cell and the pneumatic flow control is used for either rheometry or a cuvette flow cell. The details for the small volume capillary rheometry are given in ref. 28 with the addition of the syringe dilution as shown in Fig. 1.

2.1.1 Syringe-driven flow. Two syringes are used to deliver a mixture to the sample cell, one filled with a stock sample solution and another with a diluent, typically the solvent used with the stock solution. The two syringes are mounted on syringe pumps (Harvard Apparatus‡) and connected to input channels of a herringbone microfluidic mixer chip with 8 mixing cycles (Chipshop).[36] The required length of the channel for mixing depends on the Peclet number, but the repeated mixing cycles provides the necessary mixing for Peclet numbers up to approximately 10^5.[37] We adjust flow rate to target a Peclet number of approximately 10^4. The outlet from the mixing chip is connected *via* tubing (200 μm diameter tubing) to a fluidic valve and the outlet of that valve to another section of tubing to a flow cell cuvette (Hellma).

When delivering sample to the cuvette, the valve is actuated to an open position. When the specified volume has been delivered, the syringes are stopped, and the valve is simultaneously switched to a closed position to maintain a back pressure on the syringes. This eliminates flow between streams due to residual stresses or relaxation of compliance in the flow system. The valve stays in the normally closed position when there is no flow and the sample in the cuvette is being measured.

The total volume from the mixer device to a filled cuvette is approximately 300 μL. The relative flow rate of the two syringes is adjusted to deliver a new specified mixture to the sample cell. A 25 mL syringe is used for the solvent and a 5 mL syringe is used for the sample. A total volume of 500 μL is specified for delivery to the sample cell, although this volume is increased whenever necessary to satisfy a minimum dispensed volume of 10 μL from the sample syringe. The concentration sequence is performed from lowest to highest concentration to provide improved fluid displacement with increasing fluid viscosity. The total volume of samples used depends on the resolution of concentrations desired. For example, a logarithmic sequence of concentrations from an initial volume fraction of 0.01 to 1 with 5 points per decade uses about 3 mL of sample.

2.1.2 Pneumatic flow. A pneumatically controlled sample delivery method is developed for smaller-volume applications where repeated dilution and fillings of the flow cell can occur without sample degradation. This method requires an initial sample volume of approximately 100 μL to 300 μL to fill the

‡ Certain commercial equipment, instruments, software or materials are identified in this presentation to foster understanding. Such identification does not imply recommendation or endorsement by the National Institute of Standards and Technology, nor does it imply that the materials or equipment identified are necessarily the best available for the purpose.

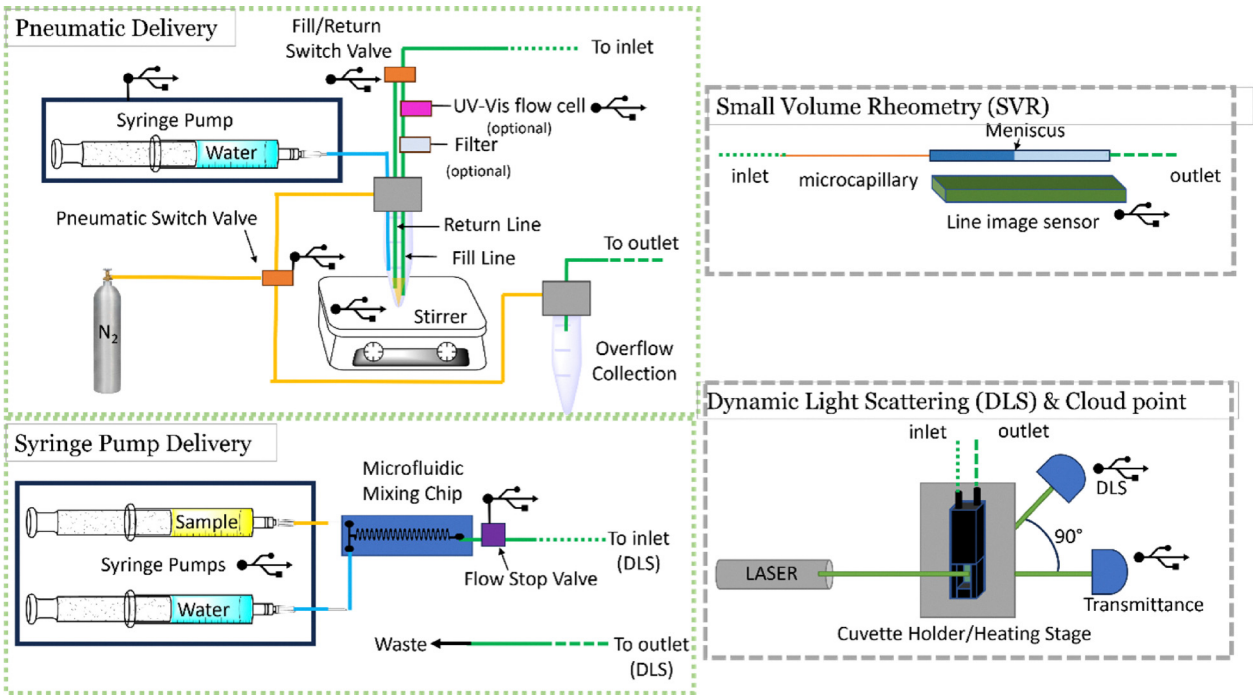

Fig. 1 Experimental setups for pneumatic delivery and syringe delivery. Specified volumes from each syringe are injected into a mixing chip before being delivered to a cuvette flow cell. Pneumatically driven flow setup delivers the sample from a reservoir to a cuvette flow cell or microcapillary. The sample is returned to the reservoir and the sample is diluted using solvent from a syringe pump.

tubing and flow cell. The sample is loaded into a reservoir, typically a 15 mL vial. The reservoir is fitted into a cap with three fluidic tubing ports and a pneumatic port for pressurizing the reservoir (Fig. 1). One section of poly(tetrafluoroethylene) tubing (1.59 mm outer diameter) extends from one port and is immersed in the sample at the bottom of the reservoir for delivery to the sample cell. Another port connects a shorter piece of tubing for return flow to the top of the reservoir above the sample level throughout the dilution sequence. This eliminates the possibility of bubbling in the sample, which may cause aggregation or other degradation of the sample. Both sections are connected to a fluidic valve that switches to deliver flow either to or from the reservoir. The sample is then driven through a section of tubing connected from the valve outlet to fill a measurement cell by pressurizing the reservoir to approximately 50 kPa with a pressure controller (Enfield). In this case it is connected to either the SVR or DLS setup.

For the DLS setup, the flow cell is placed in the temperature-controlled cuvette holder in the dynamic light scattering setup. The filling level of the flow cell is accomplished by monitoring the transmission intensity as the meniscus passes by the beam. A rapid drop in intensity triggers the system to stop after a specified delay time, typically about 5 s. The measurement step is to perform DLS measurements at fixed temperatures and specified durations, typically 5 min. Another temperature equilibration period of at least 5 min is included before the correlator is reset and autocorrelation data is obtained from the equilibrated sample. A sequence of measurements at four different temperatures takes approximately 1 hour to complete.

For the SVR, the sample is driven through a microcapillary and then to a glass capillary where the meniscus is tracked by a line image sensor, see Fig. 1. The direction of pressure drop is reversed with the pneumatic switch value to maintain the meniscus position above the image sensor. The sample viscosity is measured as a function of shear rate by adjusting the pressure drop and tracking the velocity of the meniscus to determine the flow rate.[28] The entire apparatus is enclosed in a temperature controlled box and a similar 5 min equilibration period is included before starting the viscosity measurement. The duration of the measurement depends on the viscosity of the sample and the resulting flow rate. For example, the measurement can take approximately 1 hour for high viscosity samples and as little as 5 min for low viscosity samples.

After either measurement technique has concluded, the sample is returned to the reservoir by pressurizing an empty reservoir downstream of the flow cell. The sample is diluted from a solvent line connected to a syringe pump which delivers a specified amount of solvent to the reservoir through the third port. A stir bar is placed in the reservoir and the reservoir is placed on a magnetic stirrer and stirred for approximately 5 min. After solvent is delivered to the reservoir for a dilution step, the sample is delivered to the flow cell and then immediately returned to the reservoir to mix any sample remaining in the fluidic lines.

The overall duration of the measurements depend on the number of variable experimental conditions to be tested, *e.g.* temperature, ramp rate, and concentration. Most of the examples shown in the results take between (6 to 12) hours to complete.

2.2 Temperature ramps and dynamic light scattering

Either method described above is used to fill a flow cell (Hellma model) mounted in a Quantum Northwest q-Pod unit with ±0.1 °C precision with a Quantum Northwest TC125 temperature controller. Temperature-dependent dynamic-light-scattering measurements (I_0) at a scattering angle of 90° were conducted with a solid-state laser vertically polarized with wavelength (λ) of 532 nm operating at 100 mW with power adjusted by neutral-density filters. The transmitted laser intensity was recorded by a Thorlabs PM100D photodiode. The 90° scattered light passed through a vertically polarized analyzer was collected by a lens that focuses on a single-mode fiber optic with signal split to separate single-photon counting modules and cross correlated by a Brookhaven Instruments correlator (TurboCorr), obtaining the average static scattered intensity and normalized intensity–intensity cross correlation function $g^{(2)}(q, \tau) - 1$.

The diffusion coefficient is determined from fitting of the DLS intensity–intensity time-correlation function, $G^2(q, \tau)$. This function is related to the normalized electric-field time-correlation function, $g^{(1)}(q, \tau)$ by: $G^{(2)}(q, \tau) = A(1 + \beta|g^{(1)}(q, \tau)|^2)$, where A is the average baseline intensity and β is an instrument spatial coherence factor. Depending on the composition of the solution, multiple decay modes may be present. In the case of one average relaxation mode, the electric–field correlation function is given by, $g^{(1)}(q, \tau) = (e^{-\Gamma\tau})$, where $\Gamma = Dq^2$ and D is the diffusion coefficient. The scattering vector is defined as $q = \left(4\frac{\pi n}{\lambda}\right)\sin\left(\frac{\theta}{2}\right)$, where n is the index of refraction of the solvent and θ is the scattering angle of 90°.

Two modes of operation are used to investigate the sample phase behavior. A temperature ramp is performed while the transmission and scattering intensity are recorded. The starting temperature within a one-phase region and the different ramp rates are input variables for a sequence of measurements. The ramp is interrupted when the transmission intensity reaches a near-zero threshold value, typically less than ($I/I_0 = 10^{-3}$). For multiple ramp rates, the sample is brought back to the initial temperature and held at that temperature for a specified duration, typically at least 5 min, to reach an equilibrium phase. For a subsequent specified concentration, the sample is replaced, and the temperature ramp sequence is repeated. The acquisition of the DLS signal can also be recorded over intervals to provide a quasi-steady-state cross-correlation measurement, assuming the temperature ramp rate is sufficiently slow.

DLS measurements can also be recorded at fixed temperatures after equilibrating for a predetermined time at the specified temperature. These fixed-temperature measurements can be performed with a programmed ramp sequence at a given concentration.

2.3 Polymers

Polymers were synthesized using aqueous reversible addition–fragmentation chain transfer (RAFT) methods reported previously.[38] The following were added into a 500 mL Schlenk flask: NIPAM (monomer, 40.0 g, 0.353 mole), 4-cyano-4(ethylsulfanylthiocarbonylsulfanyl)-pentanoic acid (CCP) (chain transfer agent, 0.724 g, 2.35 mmol), 2,2′-azobis[2-(2-imidazolin-2-yl)propane]dihydrochloride (VA-044) (azo initiator, 1.523 g, 4.71 mmol), benzene sulfonic acid (3.0 g), and 300 mL of deionized water. The flask was charged with a stir bar and sealed with a rubber septum. The flask was placed into an ice bath and the contents were purged with ultra-high purity argon for 1 h. The flask was placed into a water bath at 21 °C to commence the polymerization. After 10 h, the flask was removed from the water bath and immediately placed into an ice bath to quench the polymerization. The solution was transferred to a 500 mL round bottom flask and then warmed up to 40 °C using a rotary evaporation bath without applying vacuum. The polymer precipitated and the water was decanted away. The remaining polymer was then dissolved in acetone followed by precipitation from diethyl ether three times before a final wash in diethyl ether. The final product was then dried under high vacuum overnight resulting in a yellow powder.

UV-vis spectroscopy is used to characterize the concentration of pNIPAM by tracking the value at 309 nm, corresponding to the absorbance by the trithiocarbonate chain end. The samples are filled through the flow cell with a 3 mm path length.

2.4 Proteins

The protein solutions composed of IgG1 antibodies (molar mass of 150 kDa; and provided by AstraZeneca) at 233.5 mg mL^{-1} in 20 mmol L^{-1} histidine buffer were filtered with 0.2 μm, 500 μL low protein binding centrifuge filters. The concentration of protein, initially and after each dilution with 20 mmol L^{-1} histidine buffer, was determined by the absorbance at 280 nm using an in-line cross channel (Ocean Optics), with a 0.96 mm path length.

2.5 Cleaning procedures

The following procedure is used to clean the fluidic lines and glass surfaces in the various experimental setups. For pneumatically driven flow, the sample reservoir is loaded with cleaning solution and the test device (*e.g.* cuvette or capillary) is filled, allowed to soak for a specified amount of time, and returned to the reservoir. For syringe driven flow, the sample syringes are removed and syringes loaded with cleaning solution are used to drive flow through the various tubing sections. After an automated run, the sample is removed and deionized water is used to rinse the sample. A liquid alkaline cleaning solution at a volume fraction of 2% (Hellmanex) is then loaded, allowed to soak for up to 30 minutes, and then removed. The test section is then rinsed again with water using at least 10 repeated filling/unloading steps. The flow path is then dried using filtered nitrogen. For DLS measurements, the cleanliness is assessed by filling the cell with deionized water or buffer to verify that there is no scattering from contaminants. For SVR measurements, a smooth transit of the meniscus is verified using deionized water or buffer while any irregular motion of

the meniscus indicates that the surfaces are contaminated. The cleaning procedure is repeated if contaminants are detected and an additional cleaning step using isopropanol is included if required.

3 Validation

The linear scaling of absorbance with polymer concentration provides a means of comparing with control experiments, which are pre-diluted samples at the same nominal concentrations, see Fig. 2. The individual control samples also have uncertainty in concentration from preparation and handling. We quantify the deviation of the automated samples both in comparison to the measured values of the control and deviations from a linear fit through the sample measurements.

The measured absorbance for the syringe delivery shows an average absolute deviation from the linear fit to the mean syringe data within 3%. In comparison to the control experiments, a systematic offset of approximately −5% is measured. This deviation from the control experiments may result from discrepancies from nominal values in the displacement of the syringe pumps, compliance in the flow system, or the dilution of the control samples.[39] A smaller portion of this uncertainty may arise from the volume in the syringe, which is expected to be less than 1% of the nominal volume (Hamilton). The relative standard deviation for each concentration is shown based on 7 repeats of syringe dilution protocol. The relative standard deviation decreases with concentration, which may in part be due to the sensitivity of the UV-vis measurement at low concentrations, but also shows that diluting to a small fraction of a stock solution results in more variability.

For the pneumatic flow delivery method, a similar average absolute deviation of up to approximately 7% is observed in comparison to a linear fit to the data; see Fig. 2b. The largest deviation occurs at intermediate concentration values. This may be due to insufficient mixing of the sample in the lines with the newly delivered solvent, resulting in a slightly higher concentration than expected. The relative standard deviation shows a similar magnitude of variation of up to approximately 6%.

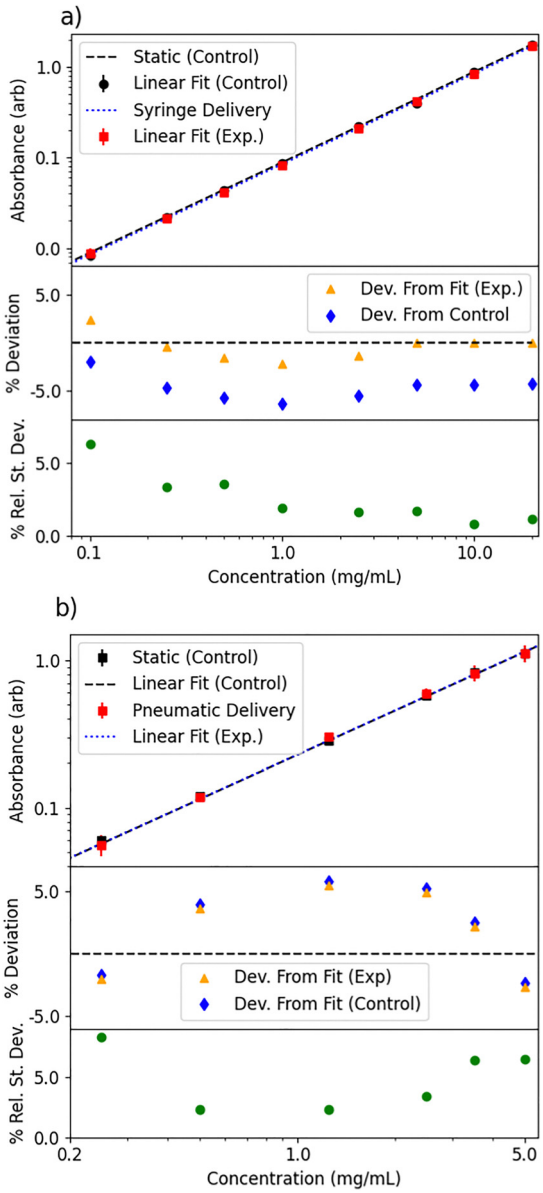

Fig. 2 Absorbance from UV-vis measurements of the pNIPAM measured at 309 nm as a function concentration using (a) the syringe delivery and (b) pneumatic delivery. Top panel shows the static control concentrations compared to the automated delivery absorbance values. The middle panel shows the percent deviation between the absorbance value and the linear fit (yellow) or the control values (blue). The bottom panel shows the relative standard deviation for the set measurements at each concentration.

4 Results

4.1 pNIPAM

The cloud point of pNIPAM (relative mass-average molar mass M_W = 12.2 kDa) was determined by the temperature at a 50% transmittance, for both statically prepared and syringe-delivered samples. A ramp rate of 1 °C min^{-1} was used for determining the cloud point, starting from 25 °C. Fig. 3a shows the transmittance as a function of temperature with a clear indication of a phase transition. We note that a cloud point assigned using a maximum gradient analysis yields similar values.

The data of syringe-delivered and statically prepared samples agree within the uncertainty estimated based on the approximately 5% average absolute deviation in concentration observed from UV-vis measurements (see Fig. 3b). Since the cloud point diverges as concentration approaches zero, the sensitivity of the concentration on the cloud point is larger at low concentrations. To characterize this, a piecewise spline is used to estimate the slope of the cloud point as a function of concentration. The uncertainty in concentration is multiplied by the slope of the fit to estimate the uncertainty in the cloud point. The uncertainty for the cloud point values is thus much

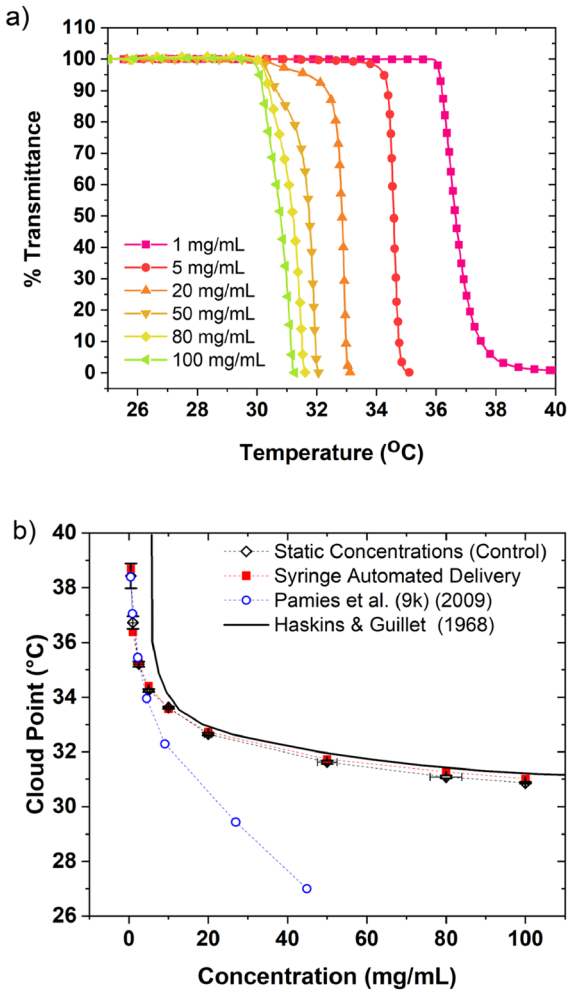

Fig. 3 (a) Transmittance as a function of temperature for different concentrations using the syringe delivery method. (b) The cloud point determined by the temperature at 50% transmittance for premixed samples compared to the delivery by automation. *x*-Axis error bars indicate a 5% uncertainty in concentration and the *y*-axis error bars indicate the corresponding uncertainty propagated to the cloud point temperature using the slope of mean cloud point values and the concentration uncertainty.

more significant at low concentrations. When compared to the literature, the cloud point of pNIPAM is similar to the Heskins and Guillet data at high concentration and Pamies *et al.* at low concentration.[3,40–42] We note that differences in molar mass and distribution, synthesis methods, and the influence of kinetics make precise comparisons of cloud point temperatures challenging.[3]

4.2 pAPAPS

The automation protocols offer more detailed measurements by combining DLS and estimates of the phase boundary through transmission intensity. This was applied to a pAPAPS polyzwitterion system with an upper critical solution temperature (UCST) to show the effects of temperature ramp rate on cloud point measurements with simultaneous DLS measurements. The number of aqueous polymer systems that display UCST behavior are limited, and the properties of these systems have important implications for drug delivery vehicles.[43–47]

The pneumatic delivery approach was used with an initial sample of 300 μL of 200 mg mL^{-1} pAPAPS stock solution. The transmission as a function of temperature and the cloud points determined from the 50% transmittance criteria are shown in Fig. 4a for a sample with M_W = 20.3 kDa. As with many thermoresponsive systems, slow kinetic transitions can significantly affect the cloud point temperature measurement.[48] In the case of this UCST system, specifically, the observed cloud point lowers progressively when the cooling rate is faster. To explore the effect of ramp rate, the temperature ramps are repeated at ramp rates from (−1.0 to −0.05) °C min^{-1}. A linear dependence on the ramp rate with measured cloud point is observed, shown for 125 mg mL^{-1} M_W = 43.2 kDa sample in Fig. 4c. Although this may not be true for all systems, a sampling of different ramp rates may be used to improve the estimate of the cloud point. The UCST from the cloud point measurements extrapolated in this way is 11 °C at a concentration of 70 mg mL^{-1}.

DLS measurements during the temperature ramp are treated as quasi-isothermal due to the slow ramp rate compared to the acquisition time (10 s). Measurements are shown for c = 50 mg mL^{-1} during the temperature ramp in Fig. 5. An acquisition is taken every 10 s over a period of 10 min, and the average temperature is reported. The correlation data shows an increase in the apparent hydrodynamic radius, $R_{h,app}$, when temperature decreases. Near a phase transition (critical point), scattering from concentration fluctuations can spatially extend and approach the wavelength of light. In this scenario, one expects a decrease in transmittance and increase in the dynamic correlation length (apparent hydrodynamic radius) and scattered intensity as the phase transition is approached.[46] These critical concentration fluctuations relax more slowly, leading to an increase in the apparent hydrodynamic radius. A decrease in the intercept for $g^2(q, \tau) - 1$ at lower temperatures is also observed due to multiple scattering effects. In the present case, the polymer chain dimension is smaller than the wavelength of light, but the scattering near the critical point can create multiple scattering effects. Strong multiple scattering is also expected in higher concentration solutions and with larger particles as the forward-scattered light performs a random walk. This leads to faster relaxation times and smaller apparent hydrodynamic radius because the critical parameter becomes related to the ratio of the path length traveled and the mean free path.[49] The effect can be mitigated by systematically reducing the path length, a technique routinely used in commercially available instruments.[50,51] Alternatively, the field of diffusing wave spectroscopy (DWS) takes advantage of multiple scattering to characterize particle dynamics.[49] Ultimately, the identification of multiple scattering artifacts must be considered on a case-by-case basis and during data analysis to avoid incorrect conclusions.[52] A second experimental approach to suppress such artifacts from scattering in turbid media

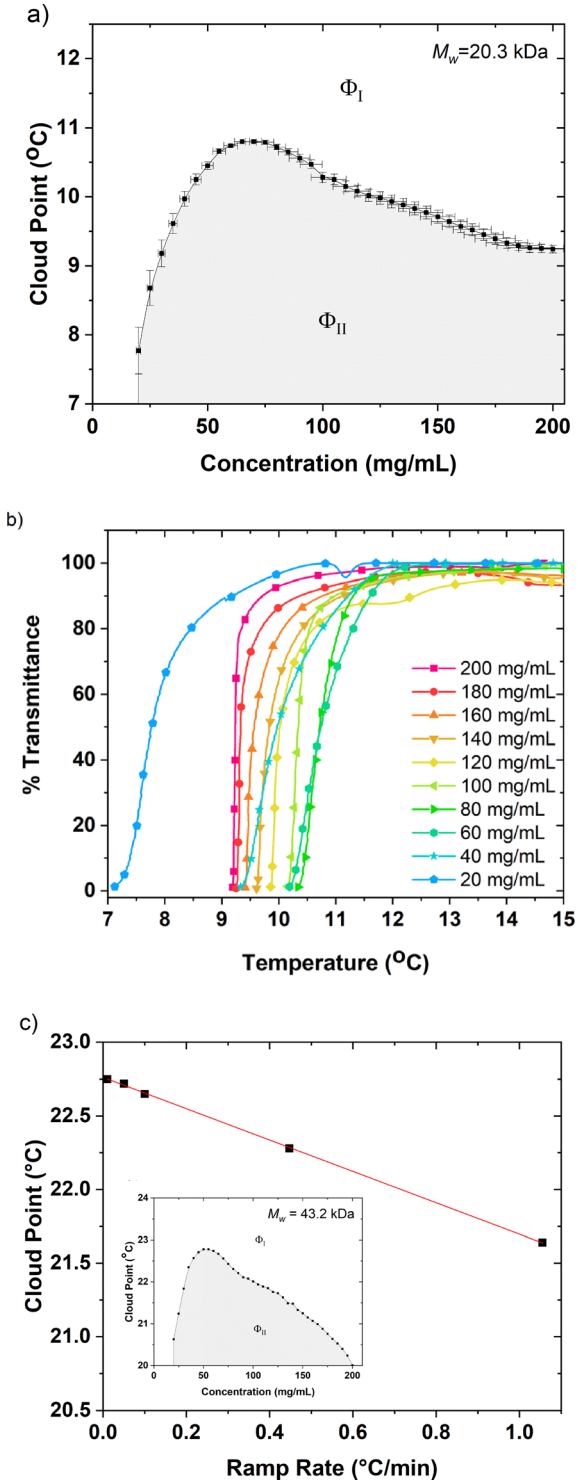

Fig. 4 (a) Cloud point values for pAPAPS (M_W = 20.3 kDa) polyzwitterion as a function of concentration at −1 °C min^{-1}. (b) Transmittance curves as a function of temperature for pAPAPS (M_W = 20.3 kDa). (c) The cloud point measurement as a function of ramp rate for 125 mg mL^{-1} pAPAPS (M_W = 43.2 kDa). The uncertainty in concentration presented a 5% value and the uncertainty in cloud point is a propagation determined from the local slope of the curve.

incorporates multi-beam and cross-correlation strategies, such as the 3D-DLS.[53–55]

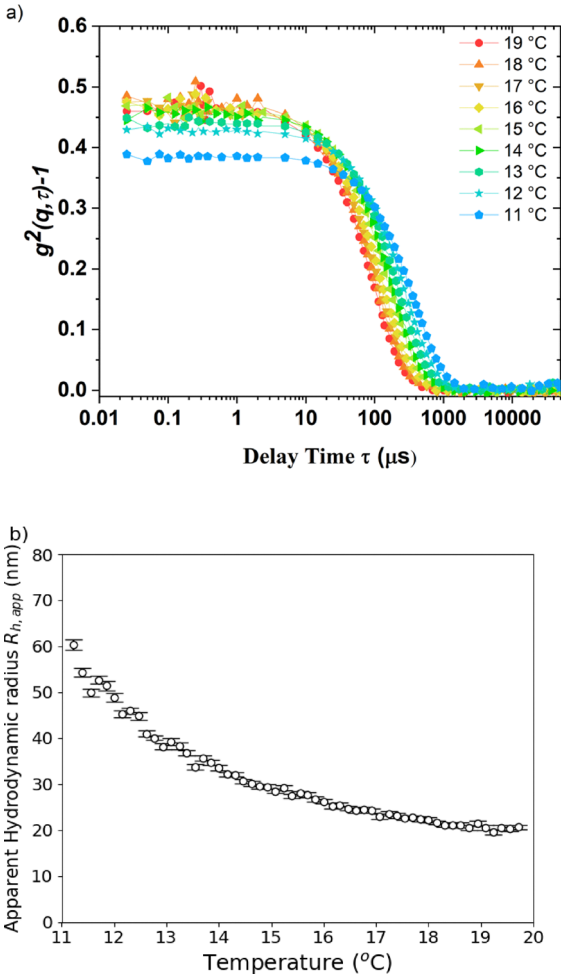

Fig. 5 (a) Dynamic light scattering of pAPAPS (M_W = 20.3 kDa) during time segments of the temperature ramp decreasing from 20 °C at −1 °C min^{-1} for the concentration 50 mg mL^{-1}. (b) The apparent hydrodynamic radius, $R_{h,app}$, calculated as a function of temperature. The error bars, obscured by the markers, show the uncertainty of $R_{h,app}$ from a single exponential fit.

4.3 Polyzwitterion-*block*-pNIPAM copolymer

DLS measurements at temperatures below the cloud point provide microstructure changes with increasing temperature as shown by the evolution of the autocorrelation function in Fig. 6b. A regularization method, known as CONTIN, was used to analyze the DLS data in terms of size distribution as shown in Fig. 6d.[56] A single mode with an ≈10 μs characteristic timescale is observed at low temperature and indicative of dispersed single chains. CONTIN validated a single mode behavior at temperatures up to approximately 34 °C.[57] Above approximately 36 °C, the dynamics become slower and exhibit a multimodal response characteristic of a critical micelle temperature (CMT).[58] The detection of the slow mode occurs at approximately (2 to 4) °C above the cloud point of the pNIPAM homopolymer, but below the cloud point for the block copolymer. The formation of micelles occurs at the CMT at a temperature below the phase transition. An increase in the hydrodynamic radius from the fast mode is observed above this temperature, indicating a change in the microstructure due

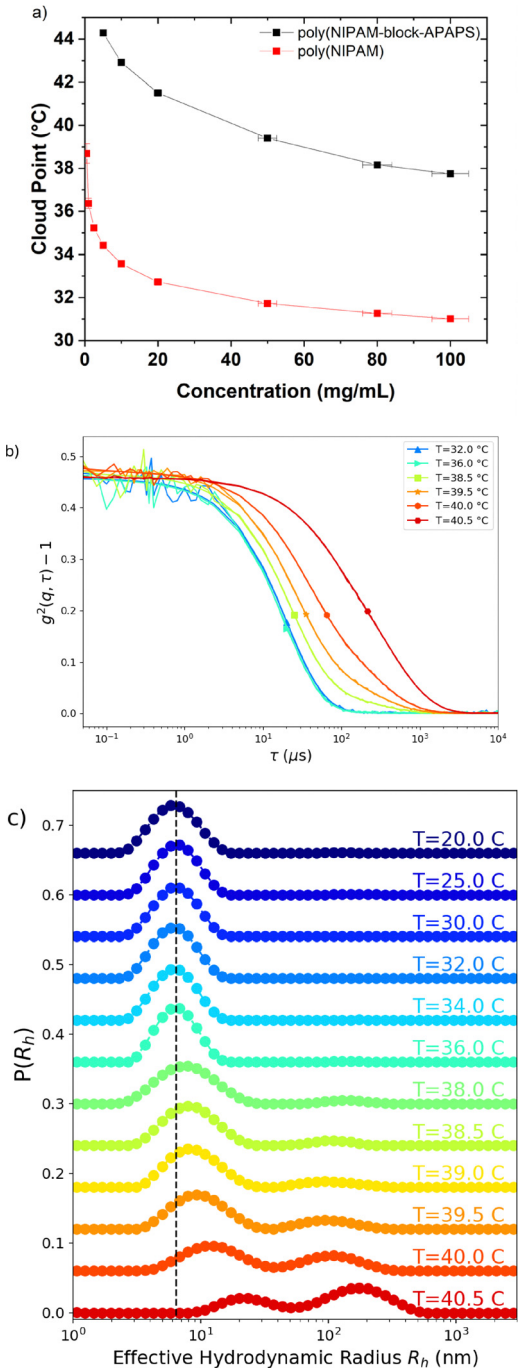

Fig. 6 (a) Poly(NIPAM-*b*-APAPS) cloud point values for the block copolymer in comparison with pNIPAM data. The uncertainty in concentration presented a 5% value and the uncertainty in cloud point is a propagation determined from the local slope of the curve. (b) DLS measurements for c = 10 mg mL^{-1} at different temperatures below the cloud point. (c) Probability distributions, for data shown in (b), as a function of effective hydrodynamic radius from the CONTIN method. We note that all of the data shown are in the single phase region. Each distribution is shifted by 0.06.

to association. This slow-mode appears as a population of larger aggregates with an R_h of ≈200 nm. The relative intensity of the slower mode also increases with temperature and becomes the dominant mode above approximately 40 °C, which is ≈3 °C below the cloud point temperature. This system shows some similar micelle formation characteristics detected in other thermoresponsive block copolymers, such as poly(methoxy diethylene glycol acrylate)-*b*-polystyrene by Kyriakos, *et al.*, but only small variation in R_h of the monomer and micelles with the temperatures that were observed in this system.[59]

4.4 Monoclonal antibody protein solutions

The interactions between proteins in solution are commonly characterized by the change in viscosity and diffusion coefficient as a function of concentration in the dilute solution limit, typically less than 10 mg mL^{-1}.[60] Similar to the polymer systems, the concentration is measured using an in-line UV-vis flow cell connected *via* optical fiber to a spectrometer (Ocean optics). A calibration of the concentration of monoclonal antibody protein is determined by the absorbance at 280 nm using protein solutions of known concentration as a reference, see Fig. 7a. During a sequence of dilutions using the reservoir setup the absorbance is recorded. A comparison of the measured concentration with the nominal concentration from successive dilutions is shown in Fig. 7b. The absorbance curves were corrected for scattering contributions from uv-degraded material using a linear scattering correction from the non-absorbing region (320 nm to 350 nm) following the approach of Thakkar *et al.*[61] A slightly lower than expected protein concentration is observed in the first dilution, but then a linear response close to the expected value is observed for subsequent dilutions. The slight deviation at the first dilution may be a result of incomplete mixing throughout the system.

The relative viscosity is measured using small volume capillary rheometry[28] over a range of shear rates (100 to 10 000) s^{-1} for four temperatures, (6.0, 14.0, 22.0 and 30.0) °C. The viscosity did not change with shear rate indicating Newtonian behavior. The mean value and uncertainty associated with each measurement is shown as a function of concentration for different temperatures. The viscosity (η) is normalized by the measured buffer solution viscosity (η_0) at each temperature and shown as a function of concentration in Fig. 8. At low concentrations, the increase in viscosity with concentration can be characterized by the intrinsic viscosity,

$$[\eta] = \lim_{c\to 0} \frac{\eta - \eta_0}{\eta_0 c}, \quad (1)$$

where η_0 is the buffer viscosity at zero solute concentration, while at higher concentrations a nonlinear increase in viscosity is observed.[62,63] This increase can be compared to the Ross–Minton equation that describes the increase in viscosity in terms of an exponential increase,

$$\frac{\eta}{\eta_0} = \exp\left[\frac{[\eta]c}{1 - \frac{k}{\nu}[\eta]c}\right], \quad (2)$$

where k is the crowding factor and ν is the Simha shape parameter.[64] The fits to the data using this equation are shown

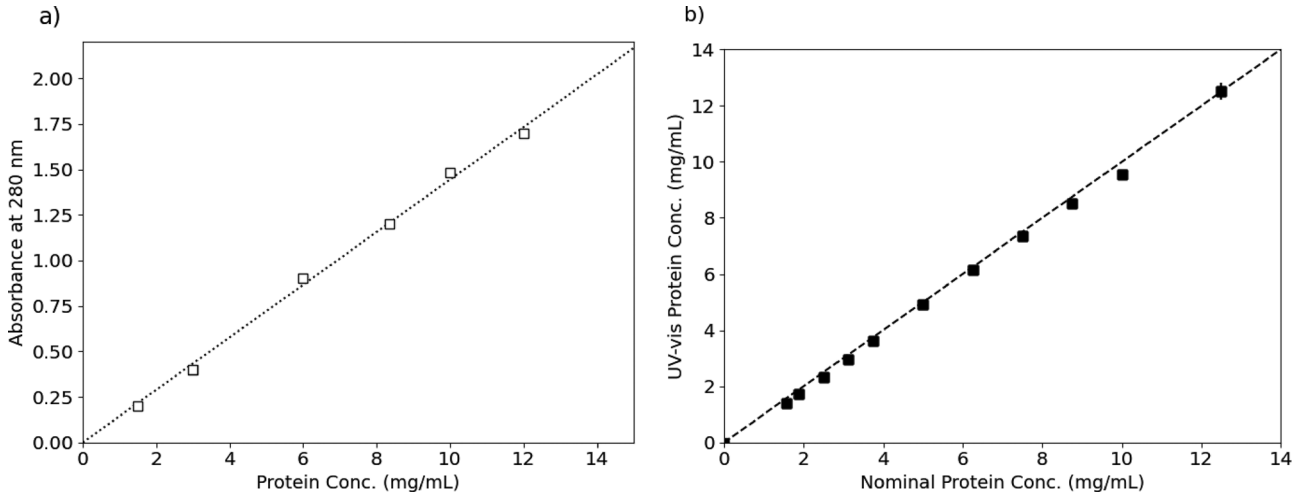

Fig. 7 (a) Calibration of protein concentration absorbance at 280 nm as a function of reference protein concentration. The line shows the linear fit. (b) Protein concentration measured from in-line UV-vis measurements as a function of nominal concentration for each dilution step. The line shows the nominal equal to the measured from the initial concentration of 12.5 mg mL^{-1}. Uncertainties (error bars) are comparable to the size of the markers and represent one standard deviation of repeated measurements at each concentration (N = 4) and uncertainty from the linear scattering correction.

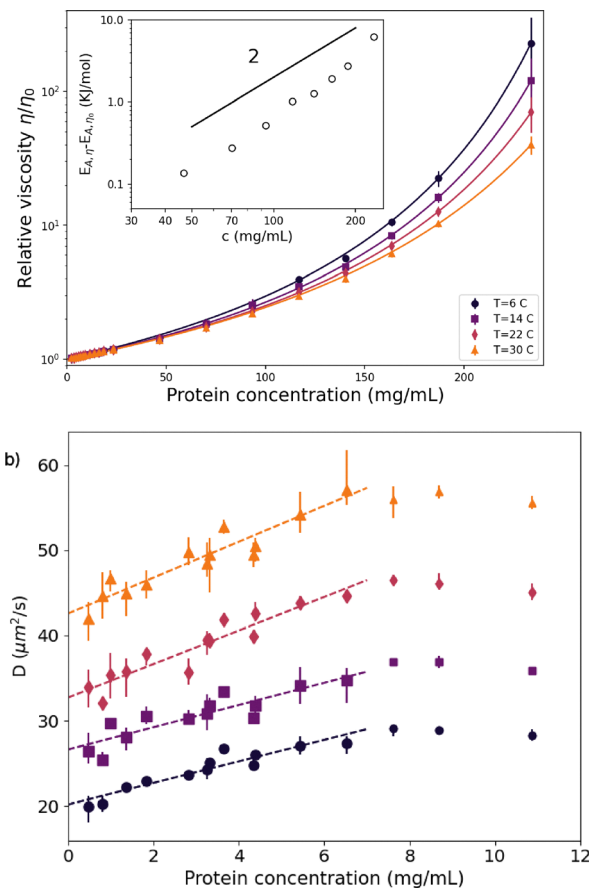

Fig. 8 Protein interactions measurements. (a) Viscosity as a function of protein concentration for four different temperatures. (b) Measured diffusion coefficient from DLS as a function of protein concentration.

in Fig. 8a and the fitted values are given in Table 1. The temperature dependent viscosity is related to the activation

Table 1 Fitted values for intrinsic viscosity, interaction parameter from the Ross–Minton equation

T (°C)	$[\eta]$ (mL g^{-1})	k/ν	k_D (mL g^{-1})
6	7.76 ± 0.05	0.367 ± 0.004	9.5 ± 4.0
14	7.07 ± 0.04	0.396 ± 0.003	17.4 ± 4.3
22	6.74 ± 0.03	0.399 ± 0.003	33.7 ± 6.4
30	6.74 ± 0.03	0.364 ± 0.003	29.2 ± 3.6

energy of viscous flow. This can be modeled with the Andrade–Eyring equation:[65–67]

$$\eta = A \exp\left(\frac{E_{A,\eta}}{RT}\right), \quad (3)$$

where $E_{A,\eta}$ is the activation energy of viscous flow, R is the gas constant, and A is a pre-exponential term. The activation energy related to the protein–protein interactions is found by subtracting the solvent contribution to the activation energy, E_{A,η_0}. At high concentrations, this activation increases with concentration by a power law of approximately 2, see inset of Fig. 8a. This scaling has been seen in other monoclonal antibodies over a similar concentration range.[68]

Another measure of protein–protein interactions is the change in the diffusion coefficient as a function of concentration using the reservoir dilution with DLS. The pneumatic delivery system, shown in Fig. 1b, is modified to include a low protein binding filter in an outlet stream from the reservoir to remove aggregates that can develop in the reservoir during mixing.

Protein–protein interactions are characterized by a first-order virial correction to the diffusion coefficient, $D(c) = D_0(1 + k_D c)$, where k_D is the interaction parameter. The diffusion coefficient is shown in Fig. 8b for four different temperatures. The dilution starts from a sample with a concentration of 12.5 mg mL^{-1} and is diluted 10 times to <2 mg mL^{-1}. Linear fits to the data below

8 mg mL^{-1} are shown for the measurement of k_D, which increases with increasing temperature. A plateau in the diffusion coefficient is observed for higher concentrations above approximately 10 mg mL^{-1}.

5 Conclusions

We present two different automated sample mixing and delivery methods for small volume characterization using DLS or microcapillary rheometry. The two methods provide an automated and repeatable method for delivering diluted samples to a spectroscopic flow cell. In-line UV-vis absorbance spectroscopy measures the concentration at each dilution step. These concentrations compare to the commanded concentration within about 3% for the syringe delivery and 5% for the pneumatic delivery. The dilution reservoir measurements required approximately 200 μL of high concentration ($c > 200$ mg mL^{-1}) sample for the viscosity measurements and approximately 450 μL of low concentration ($c < 12$ mg mL^{-1}) sample for the DLS measurements.

The two fluid delivery methods each have advantages and drawbacks. The syringe delivery provides accuracy within the tolerance of the displacement of the volume within the syringes. This is subject to uncertainties of syringe diameter and displacement, which are in the range of 1% to 3%.[39,69,70] The primary disadvantage of the syringe delivery is the larger sample volume for each dilution, approximately 500 μL total volume, due to the need to replace the sample in the flow cell with each new solution. The volume of stock sample is therefore mostly dependent on the number of measurements required at high volume fractions of the stock. The main advantage of the reservoir approach is the small total sample required, approximately 200 μL, while the main disadvantage is the accuracy of the concentration. The reservoir approach is sensitive to uncertainties in the sample preparation, including the initial sample volume in the reservoir, which leads to a propagated uncertainty through the successive dilutions. Also, complete mixing of the sample in the flow lines requires multiple exchanges between the fluid in the lines and the reservoir. These exchanges also present potential issues with residual fluid in the lines due to fluid film formation while air displaces the fluid in the lines. These uncertainties are most significant when the amount of diluent is small compared to the total initial sample volume. Another source of uncertainty is evaporation of the sample. This is minimized by providing saturated gas in the pneumatic lines using in line water-filled reservoirs, but long duration measurements may lead to some evaporation, particularly if the reservoir must be heated above room temperature to maintain a mixed sample. Despite the additional uncertainties concerning sample concentration with the pneumatic approach, these uncertainties are substantially reduced when the concentration can be measured directly with inline UV-vis spectroscopy, as done here.

The appropriate approach for a given sample and diluent must be determined based on the needs for accuracy of concentration and the total volume of sample available. Both approaches are suitable for different types of characterization methods, such as small angle neutron scattering, small angle light scattering, *etc.* The benefits of either automated approach can be offset somewhat by more difficult cleaning procedures and setup times, and therefore are most advantageous for large numbers of sample conditions. These methods can also be extended to multicomponent solutions, higher temperature measurements, and automated cleaning.

Conflicts of interest

There are no conflicts to declare.

Data availability

Data for this article, including comma separated value (CVS) files are available at the NIST public data repository at https://doi.org/10.18434/mds2-4184.[71]

Acknowledgements

A portion of this work was performed under a Cooperative Research and Development Agreement (CRADA) no. CN-14-0046 between the National Institute of Standards and Technology (NIST) and AstraZeneca PLC. The contributions of C. M. were supported by a Summer Undergraduate Research Fellowship at NIST.

References

1 P. A. Beaucage, D. R. Sutherland and T. B. Martin, *Macromolecules*, 2024, **57**, 8661–8670.
2 S. Ali, Y. Mao and V. M. Prabhu, *Rev. Sci. Instrum.*, 2022, **93**, 44104.
3 A. Halperin, M. Kröger and F. M. Winnik, *Angew. Chem., Int. Ed.*, 2015, **54**, 15342–15367.
4 Y. Ma, S. Ali and V. M. Prabhu, *Macromolecules*, 2021, **54**, 11338–11350.
5 P. G. Vekilov, *J. Phys.: Condens. Matter*, 2012, **24**, 193101.
6 T. B. Martin and D. J. Audus, *ACS Polym. Au*, 2023, **3**, 239–258.
7 M. Christensen, L. P. Yunker, P. Shiri, T. Zepel, P. L. Prieto, S. Grunert, F. Bork and J. E. Hein, *Chem. Sci.*, 2021, **12**, 15473–15490.
8 N. Hartrampf, A. Saebi, M. Poskus, Z. P. Gates, A. J. Callahan, A. E. Cowfer, S. Hanna, S. Antilla, C. K. Schissel, A. J. Quartararo, X. Ye, A. J. Mijalis, M. D. Simon, A. Loas, S. Liu, C. Jessen, T. E. Nielsen and B. L. Pentelute, *Science*, 2020, **368**, 980–987.
9 B. Lin, J. L. Hedrick, N. H. Park and R. M. Waymouth, *J. Am. Chem. Soc.*, 2019, **141**, 8921–8927.
10 O. Weismantel, L. J. Weerarathna and T. Junkers, *ACS Appl. Polym. Mater.*, 2025, **7**, 938–947.

11 M. Alexovič, B. Horstkotte, I. Šrámková, P. Solich and J. Sabo, *TrAC, Trends Anal. Chem.*, 2017, **86**, 39–55.
12 N. Amornthammarong, P. B. Ortner and J. Z. Zhang, *Talanta*, 2010, **81**, 1472–1476.
13 B. Horstkotte and P. Solich, *Molecules*, 2020, **25**, 1612.
14 N. Manousi, A. Kabir, K. G. Furton and A. N. Anthemidis, *Anal. Chem.*, 2022, **94**, 12943–12947.
15 K. Dauer, S. Pfeiffer-Marek, W. Kamm and K. G. Wagner, *Pharmaceutics*, 2021, **13**, 172.
16 P. A. Beaucage and T. B. Martin, *Chem. Mater.*, 2023, **35**, 846–852.
17 F. Geißler, M. Martínez-Cabanas, P. Lodeiro and E. P. Achterberg, *Anal. Bioanal. Chem.*, 2021, **413**, 6889–6904.
18 N. Meulendijks, R. van Ee, R. Stevens, M. Mourad, M. Verheijen, N. Kambly, R. Armenta and P. Buskens, *Appl. Sci.*, 2018, **8**, 108.
19 T. Q. Chastek, K. Iida, E. J. Amis, M. J. Fasolka and K. L. Beers, *Lab Chip*, 2008, **8**, 950–957.
20 K. Iida, T. Q. Chastek, K. L. Beers, K. A. Cavicchi, J. Chun and M. J. Fasolka, *Lab Chip*, 2009, **9**, 339–345.
21 F. Destremaut, J. B. Salmon, L. Qi and J. P. Chapel, *Lab Chip*, 2009, **9**, 3289–3296.
22 L. M. G. Torquato, N. Hélaine, Y. Cui, R. O'Connell, J. Gummel, E. S. J. Robles, D. Jacob and J. T. Cabral, *Lab Chip*, 2023, **23**, 2540–2552.
23 R. J. Raterink, Y. Witkam, R. J. Vreeken, R. Ramautar and T. Hankemeier, *Anal. Chem.*, 2014, **86**, 10323–10330.
24 J. Y. Kim, S. J. Lee, G. Y. Baik and J. G. Hong, *ACS Omega*, 2021, **6**, 29724–29734.
25 T. Garting and A. Stradner, *Colloids Surf., B*, 2019, **181**, 516–523.
26 K. T. Lauser, A. L. Rueter and M. A. Calabrese, *Soft Matter*, 2021, **17**, 9624–9635.
27 S. F. Berlanda, M. Breitfeld, C. L. Dietsche and P. S. Dittrich, *Anal. Chem.*, 2021, **93**, 311–331.
28 P. F. Salipante, S. Kuei and S. D. Hudson, *Rheol. Acta*, 2022, **61**, 309–317.
29 D. Vloemans, A. Pieters, F. Dal Dosso and J. Lammertyn, *Lab Chip*, 2024, **24**, 2791–2801.
30 Y. Shangguan, D. Guo, H. Feng, Y. Li, X. Gong, Q. Chen, B. Zheng and C. Wu, *Macromolecules*, 2014, **47**, 2496–2502.
31 F. Shi, Z. Han, J. Li, B. Zheng and C. Wu, *Macromolecules*, 2011, **44**, 686–689.
32 C. Wu and Y. Li, *Macromolecules*, 2018, **51**, 5863–5866.
33 E. Selimović, F. Gobeaux and S. Fraden, *Lab Chip*, 2010, **10**, 1696–1699.
34 D. Yang, M. Daviran, K. M. Schultz and L. M. Walker, *Pharm. Res.*, 2021, **38**, 1765–1775.
35 S. Ashraf, H. K. Park, H. Park and S. H. Lee, *Macromol. Res.*, 2016, **24**, 297–304.
36 A. D. Stroock, S. K. Dertinger, A. Ajdari, I. Mezić, H. A. Stone and G. M. Whitesides, *Science*, 2002, **295**, 647–651.
37 M. S. Williams, K. J. Longmuir and P. Yager, *Lab Chip*, 2008, **8**, 1121–1129.
38 P. D. Pickett, Y. Ma, N. D. Posey, M. Lueckheide and V. M. Prabhu, *Macromol. Eng.*, 2022, 1–51.
39 E. Batista, M. Álvares, R. F. Martins, F. Ogheard, J. Geršl and I. Godinho, *Biomed. Tech.*, 2023, **68**, 29–38.
40 F. Afroze, E. Nies and H. Berghmans, *J. Mol. Struct.*, 2000, **554**, 55–68.
41 M. Heskins and J. E. Guillet, *J. Macromol. Sci. Chem.*, 1968, **2**, 1441–1455.
42 R. Pamies, K. Zhu, A. L. Kjøniksen and B. Nyström, *Polym. Bull.*, 2009, **62**, 487–502.
43 M. Ilčíková, J. Tkáč and P. Kasák, *Polymers*, 2015, **7**, 2344–2370.
44 K. Kuperkar, D. Patel, L. I. Atanase and P. Bahadur, *Polymers*, 2022, **14**, 4702.
45 A. Laschewsky, *Polymers*, 2014, **6**, 1544–1601.
46 B. J. Niebuur, J. Puchmayr, C. Herold, L. P. Kreuzer, V. Hildebrand, P. Müller-Buschbaum, A. Laschewsky and C. M. Papadakis, *Materials*, 2018, **11**, 850.
47 C. M. Papadakis, P. Müller-Buschbaum and A. Laschewsky, *Langmuir*, 2019, **35**, 9660–9676.
48 K. Van Durme, G. Van Assche and B. Van Mele, *Macromolecules*, 2004, **37**, 9596–9605.
49 D. A. Weitz and D. J. Pine, in *Dynamic Light Scattering: The Method and Some Applications*, ed. W. Brown, Oxford University Press, New York, 1993, ch. 16, p. 652.
50 G. Bryant and J. C. Thomas, *Langmuir*, 1995, **11**, 2480–2485.
51 R. Ragheb and U. Nobbmann, *Sci. Rep.*, 2020, **10**, 21768.
52 D. Langevin, E. Raspaud, S. Mariot, A. Knyazev, A. Stocco, A. Salonen, A. Luch, A. Haase, B. Trouiller, C. Relier, O. Lozano, S. Thomas, A. Salvati and K. Dawson, *NanoImpact*, 2018, **10**, 161–167.
53 I. D. Block and F. Scheffold, *Rev. Sci. Instrum.*, 2010, **81**, 123107.
54 A. Gulotta, M. Polimeni, S. Lenton, C. G. Starr, A. Stradner, E. Zaccarelli and P. Schurtenberger, *Mol. Pharmaceutics*, 2024, **21**, 2250–2271.
55 L. B. Aberle, P. Hülstede, S. Wiegand, W. Schröer and W. Staude, *Appl. Opt.*, 1998, **37**, 6511–6524.
56 S. W. Provencher, *Comput. Phys. Commun.*, 1982, **27**, 229–242.
57 M. Salazar, H. Srivastav, A. Srivastava and S. Srivastava, *Soft Matter*, 2023, **19**, 6535–6544.
58 P. D. Pickett, Y. Ma and V. M. Prabhu, *J. Chem. Phys.*, 2023, **159**, 104902.
59 K. Kyriakos, D. Aravopoulou, L. Augsbach, J. Sapper, S. Ottinger, C. Psylla, A. Aghebat Rafat, C. A. Benitez-Montoya, A. Miasnikova, Z. Di, A. Laschewsky, P. Müller-Buschbaum, A. Kyritsis and C. M. Papadakis, *Colloid Polym. Sci.*, 2014, **292**, 1757–1774.
60 B. D. Connolly, C. Petry, S. Yadav, B. Demeule, N. Ciaccio, J. M. Moore, S. J. Shire and Y. R. Gokarn, *Biophys. J.*, 2012, **103**, 69–78.
61 S. V. Thakkar, K. M. Allegre, S. B. Joshi, D. B. Volkin and C. R. Middaugh, *J. Pharm. Sci.*, 2012, **101**, 3051–3061.
62 A. Saluja and D. S. Kalonia, *Int. J. Pharm.*, 2008, **358**, 1–15.
63 M. A. Woldeyes, L. L. Josephson, D. L. Leiske, W. J. Galush, C. J. Roberts and E. M. Furst, *Mol. Pharmaceutics*, 2018, **15**, 4745–4755.
64 P. D. Ross and A. P. Minton, *Biochem. Biophys. Res. Commun.*, 1977, **76**, 971–976.

65 C. W. Macosko, *Rheology principles*, VCH Publishes, 1994.
66 E. D. C. Andrade, *Nature*, 1930, **125**, 309–310.
67 H. Eyring, *J. Chem. Phys.*, 1936, **4**, 283–291.
68 M. A. Woldeyes, W. Qi, V. I. Razinkov, E. M. Furst and C. J. Roberts, *Mol. Pharmaceutics*, 2020, **17**, 4473–4482.
69 E. Batista, I. Godinho, R. F. Martins, R. Mendes and J. Robarts, *Flow Meas. Instrum.*, 2020, **75**, 101789.
70 H. Bissig, M. Tschannen and M. de Huu, *Flow Meas. Instrum.*, 2020, **73**, 101729.
71 P. F. Salipante, *Data for ''Experimental Automation for High-Throughput Collection of Phase Behavior and Dynamic Light Scattering Data for Thermally-Responsive Polymers''*, National Institute of Standards and Technology, DOI: 10.18434/mds2-4184.

